Multiplicative intrinsic component optimization (MICO) for MRI bias field estimation and tissue segmentation

Chunming Li [a,*], John C. Gore [b], Christos Davatzikos [a]

[a] Center of Biomedical Image Computing and Analytics, University of Pennsylvania, Philadelphia 19104, USA
[b] Vanderbilt University Institute of Imaging Science, Vanderbilt University, Nashville, TN 37232, USA

ARTICLE INFO

ABSTRACT

This paper proposes a new energy minimization method called multiplicative intrinsic component optimization (MICO) for joint bias field estimation and segmentation of magnetic resonance (MR) images. The proposed method takes full advantage of the decomposition of MR images into two multiplicative components, namely, the true image that characterizes a physical property of the tissues and the bias field that accounts for the intensity inhomogeneity, and their respective spatial properties. Bias field estimation and tissue segmentation are simultaneously achieved by an energy minimization process aimed to optimize the estimates of the two multiplicative components of an MR image. The bias field is iteratively optimized by using efficient matrix computations, which are verified to be numerically stable by matrix analysis. More importantly, the energy in our formulation is convex in each of its variables, which leads to the robustness of the proposed energy minimization algorithm. The MICO formulation can be naturally extended to 3D/4D tissue segmentation with spatial/sptatiotemporal regularization. Quantitative evaluations and comparisons with some popular softwares have demonstrated superior performance of MICO in terms of robustness and accuracy.

1. Introduction

Image segmentation is a fundamental problem in medical image computing. In magnetic resonance imaging (MRI), segmentation is challenged by an inherent artifact, called *intensity inhomogeneity*, which manifests itself as slow intensity variations in the same tissue over the image domain. Intensity inhomogeneity in MRI may be attributed to a number of factors, including B1 and B0 field inhomogeneities and patient-specific interactions. Due to the intensity inhomogeneity, there are overlaps between the ranges of the intensities of different tissues, which often causes misclassification of tissues. Other image analysis algorithms, such as image registration, can also be misled by intensity inhomogeneities. Therefore, it is often a mandatory step to remove the intensity inhomogeneity through a procedure called *bias field correction* before performing quantitative analysis of MRI data. Bias field correction is usually performed by estimating the bias field that accounts for the intensity inhomogeneity in the MR image and then dividing the image by the estimated bias field to generate a bias field corrected image.

Traditional segmentation algorithms, such as K-means algorithm, often fail in the presence of intensity inhomogeneities in the images. To apply these algorithms, one has to perform bias field correction in a separate preprocessing step to remove the intensity inhomogeneity. Some advanced image segmentation algorithms have an internal mechanism to handle intensity inhomogeneities, and therefore can be directly used for segmentation without the need for bias field correction in a separate preprocessing step. These methods typically interleave bias field estimation and image segmentation in an iterative process.

In [1], Wells et al. developed an approach based on an expectation-maximization (EM) algorithm for interleaved bias field estimation and segmentation. This method was later improved by Guillemaud and Brady in [2]. However, these EM based methods require good initialization for either the bias field or for the classification estimate [3]. They typically require manual selections of representative points for each tissue class to perform initialization. Such initializations are subjective and often irreproducible [4]. Moreover, the final result of bias field correction and segmentation are sensitive to the specific choices of initial conditions [5].

In [6], Pham and Prince proposed an energy minimization approach for segmentation and bias field estimation in which a fuzzy c-means (FCM) algorithm was used for segmentation. Their method, called adaptive FCM (AFCM), is an extension of FCM by introducing a bias field as a factor in the cluster centers. In their energy function, a smoothing term was introduced to ensure the

smoothness of the bias field. The coefficient of the smoothing term is, however, sometimes difficult to adjust [5], which limits the utility of the algorithm. In a later paper [7], Pham extended AFCM to an improved formulation called FANTASM by adding a spatial regularization mechanism on the tissue membership functions. The spatial regularization overcomes the effect of the noise, but FANTASM still has the same problem associated with the smoothing term for the bias field as in AFCM.

Bias field correction itself is an important medical image processing task. Many bias field correction algorithms have been proposed in the past two decades. The existing bias correction methods can be broadly categorized into two classes: prospective methods [8–14] and retrospective methods [1,15–17,6,4,3,18–20]. Prospective methods try to avoid intensity inhomogeneity in the acquisition process by using special hardware or specific sequences. These methods are able to correct some of the intensity inhomogeneities caused by the MR scanner, but fail to handle the inhomogeneities that are patient dependant, which makes them of limited value for in practical applications [21]. In contrast to the prospective methods, retrospective methods rely exclusively on the information within the acquired image and thus can be applied to remove the intensity inhomogeneities caused by patient dependant effects. A recent review of bias correction methods can be found in [5].

One of the earliest retrospective methods for bias field correction is the homomorphic filtering [15]. This method assumes that intensity inhomogeneity is a low spatial frequency signal that can be suppressed by high pass filtering. However, the imaged objects themselves usually contain low frequencies as well and, as a result, filtering methods often fail to produce satisfactory bias field corrections [5]. Dawant et al. [16] proposed a method that estimates the inhomogeneity field by fitting splines to the intensities of selected points. Their method relies on manually selecting reference points inside white matter. In [17], an iterative method, called N3, based on intensity histograms was proposed for bias field correction. It aims to derive the smooth bias field that optimally sharpens the intensity histogram of the image. In [22], the implementation of the N3 algorithm was improved by using a faster and more robust B-spline approximation to compute the bias field.

In this paper, we propose a new approach for bias field estimation and tissue segmentation in an energy minimization framework. The proposed method jointly performs bias field estimation and the tissue membership functions in an energy minimization process to optimize two multiplicative intrinsic components of an MR image, the bias field that accounts for the intensity inhomogeneity and the true image that characterizes a physical property of the tissues. The spatial properties of these two components are fully reflected in their representations and the proposed energy minimization formulation. Our method, which we call multiplicative intrinsic component optimization (MICO), is robust due to the convexity of the energy function in each of its variables. The proposed MICO formulation can be naturally extended to 3D/4D segmentation with spatial/spatio-temporal regularization.

2. Multiplicative intrinsic component optimization

In this section, we present the formulation of MICO for bias field estimation and tissue segmentation based on the decomposition of an MR image into two multiplicative components. We propose an energy minimization approach to optimize these two multiplicative components, which leads to the MICO algorithm for joint bias field estimation and tissue segmentation.

2.1. Decomposition of MR images into multiplicative intrinsic components

From the formation of MR images, it has been generally accepted that an MR image I can be modeled as

$$I(x) = b(x)J(x) + n(x), \tag{1}$$

where $I(x)$ is the intensity of the observed image at voxel x, $J(x)$ is the true image, $b(x)$ is the bias field that accounts for the intensity inhomogeneity in the observed image, and $n(x)$ is additive noise with zero-mean. The bias field b is assumed to be smoothly varying. The true image J characterizes a physical property of the tissues being imaged, which ideally take a specific value for the voxels within the same type of tissue. Therefore, we assume that $J(x)$ is approximately a constant c_i for all point x in the i-th tissue. The above assumptions have been generally accepted in the literature [1,4,6].

In this paper, we consider (1) as a decomposition of the MR image I into two multiplicative components b and J and additive zero-mean noise n. From this perspective, we formulate bias field estimation and tissue segmentation as an energy minimization problem of seeking optimal decomposition of the image I into two multiplicative components b and J. We refer to the bias field b and the true image J as intrinsic components of the observed MR image I. In this paper, we view an image I as a function $I: \Omega \rightarrow \Re$ on a continuous domain Ω.

In the context of computer vision, an observed image of a scene has a similar decomposition as in (1). An observed image I can be decomposed as $I = RS$ with two multiplicative components: the reflectance image R and the illumination image S. In [23], Barrow and Tenenbaum proposed using the terms *intrinsic images* to represent these two multiplicative components. Estimation of the intrinsic images from an observed scene image has been an important problem in computer vision. Numerous methods have been proposed to estimate the intrinsic images from a scene image based on different assumptions on the two intrinsic images [24–26].

In this paper, we consider the bias field b and the true image J as the *multiplicative intrinsic components* of an observed MR image. We propose a novel method to estimate these two components from an observed MR image. We note that the method proposed in this paper is different from those methods for estimating reflectance and illumination images in computer vision. In fact, the estimation of intrinsic images is an ill-posed problem due to the lack of sufficient knowledge about the unknown intrinsic images R and S.

Estimation of the multiplicative components b and J of the observed MR image I is an underdetermined or ill-posed problem if no knowledge about them is used. To make the problem solvable, we have to use some knowledge about the bias field b and true image J. In this paper, we propose a method that uses the basic properties of the true image and bias field, namely, the piecewise constant property of the true image J and the smoothly varying property of the bias field b. The decomposition of the MR image I into two multiplicative intrinsic components b and J with their respective spatial properties are fully exploited in the formulation of our method.

2.2. Representations of multiplicative intrinsic components

To effectively use the properties of the bias field b and true image J, we need appropriate mathematical representation and description of the bias field and true image. In our method, the bias field is represented by a linear combination of a given set of smooth basis functions $g_1, \cdots, g_M$, which ensures the smoothly varying property of

the bias field. Theoretically, a function can be approximated by a linear combination of a number of basis functions up to arbitrary accuracy [27], given a sufficiently large number M of the basis functions. In the applications of MICO to 1.5 T and 3 T MRI data, we use 20 polynomials of the first three degrees as the basis functions.

The estimation of the bias field is performed by finding the optimal coefficients $w_1, \cdots, w_M$ in the linear combination $b(x) = \sum_{k=1}^{M} w_k g_k$. We represent the coefficients $w_1, \cdots, w_M$ by a column vector $\mathbf{w} = (w_1, \cdots, w_M)^T$, where $(\cdot)^T$ is the transpose operator. The basis functions $g_1(x), \cdots, g_M(x)$ are represented by a column vector valued function $G(x) = (g_1(x), \cdots, g_M(x))^T$. Thus, the bias field $b(x)$ can be expressed in the following vector form

$$b(x) = \mathbf{w}^T G(x). \tag{2}$$

The above vector representation will be used in our proposed energy minimization method for bias field estimation, which allows us to use efficient vector and matrix computations to compute the optimal bias field derived from the energy minimization problem, as will be described in Section 2.4.

The piecewise approximately constant property of the true image J can be stated more specifically as follows. We assume that there are N types of tissues in the image domain Ω. The true image $J(x)$ is approximately a constant c_i for x in the i-th tissue. We denote by Ω_i the region where the i-th tissue is located. Each region (tissue) Ω_i can be represented by its *membership function* u_i. In the ideal case where every voxel contains only one type of tissue, the membership function u_i is a binary membership function, with $u_i(x) = 1$ for $x \in \Omega_i$ and $u_i(x) = 0$ for $x \notin \Omega_i$. In reality, one voxel may contain more than one type of tissues due to the partial volume effect, especially at the interface between neighboring tissues. In this case, the N tissues can be represented by *fuzzy membership functions* $u_i(x)$ that take values between 0 and 1 and satisfy $\sum_{i=1}^{N} u_i(x) = 1$. The value of the fuzzy membership function $u_i(x)$ can be interpreted as the percentage of the i-th tissue within the voxel x. Such membership functions $u_1, \cdots, u_N$ can be represented by a column vector valued function $\mathbf{u} = (u_1, \cdots, u_N)^T$, where T is the transpose operator. We denote by $\mathscr{U}$ the space of all such vector valued functions, i.e.

$$\mathscr{U} \triangleq \left\{ \mathbf{u} = (u_1, \cdots, u_N)^T : 0 \le u_i(x) \le 1, i = 1, \cdots, N, \text{ and } \sum_{i=1}^{N} u_i(x) = 1, \text{for all } x \in \Omega \right\} \tag{3}$$

Given the membership functions u_i and constants c_i, the true image J can be approximated by

$$J(x) = \sum_{i=1}^{N} c_i u_i(x). \tag{4}$$

In the case that the membership functions u_i are binary functions, the function in (4) is a piecewise constant function, with $J(x) = c_i$ for $x \in \Omega_i = \{x: u_i(x) = 1\}$. The binary membership functions $u_1, \cdots, u_N$ represent a *hard segmentation* result, and the corresponding regions $\Omega_1, \cdots, \Omega_N$ form a partition of the image domain Ω, such that $\cup_{i=1}^{N} \Omega_i = \Omega$ and $\Omega_i \cap \Omega_j = \emptyset$. More generally, fuzzy membership functions $u_1, \cdots, u_N$ with values between 0 and 1 represent a *soft segmentation* result.

Based on the image model (1), we propose an energy minimization method for simultaneous bias field estimation and tissue segmentation. The result of tissue segmentation is given by the membership function $\mathbf{u} = (u_1, \cdots, u_N)$. The estimated bias field b is used to generate the bias field corrected image, which is computed as I/b.

2.3. Energy formulation for multiplicative intrinsic component optimization

We propose an energy minimization formulation for bias field estimation and tissue segmentation based on the image model (1) and the intrinsic properties of the bias field and the true image as described in Section 2.1. In view of the image models (1), we consider the problem of finding the multiplicative intrinsic components b and J of an observed MR image I such that the following energy is minimized

$$F(b, J) = \int_{\Omega} |I(x) - b(x)J(x)|^2 dx. \tag{5}$$

Obviously, minimization of this energy is an ill-posed problem if there are no constraints on the variables b and J. In fact, without any constraint, the energy $F(b, J)$ is minimized by any non-zero function b and $J = I/b$. To make the problem solvable, we need to confine the search spaces of b and J by exploiting some knowledge about the unknowns b and J. In fact, the properties of the bias field b and the true image J described in Section 2.1 are the knowledge that can be used to confine the search spaces of b and J to specific subspaces that reflect these properties.

Using the property that the true image J is piecewise approximately constant, we can confine the search space of the true image J to the subspace of piecewise constant functions $J(x) = \sum_{i=1}^{N} c_i u_i(x)$ as in (4) with binary membership functions $u_1, \cdots, u_N$. On the other hand, the search space of the bias field b is confined to the subspace of all the functions in the form $b(x) = \mathbf{w}^T G(x)$ as in (2). With these representations of the true image J and bias field b, the energy $F(b, J)$ can be expressed in terms of three variables, $\mathbf{u} = (u_1, \cdots, u_N)^T$, $\mathbf{c} = (c_1, \cdots, c_N)^T$, and $\mathbf{w} = (w_1, \cdots, w_M)^T$, namely,

$$F(b, J) = F(\mathbf{u}, \mathbf{c}, \mathbf{w}) = \int_{\Omega} \left| I(x) - \mathbf{w}^T G(x) \sum_{i=1}^{N} c_i u_i(x) \right|^2 dx, \tag{6}$$

Thus, the optimization of b and J can be achieved by minimizing the energy F with respect to $\mathbf{u}$, $\mathbf{c}$, and $\mathbf{w}$.

Since u_i is the binary membership function of the region Ω_i, with $u_i(x) = 1$ for $x \in \Omega_i$ and $u_i(x) = 0$ for $x \notin \Omega_i$, we have $\sum_{i=1}^{N} c_i u_i(x) = c_i$ for $x \in \Omega_i$. Therefore, the energy F can be expressed as:

$$\begin{aligned} F(\mathbf{u}, \mathbf{c}, \mathbf{w}) &= \int_{\Omega} \left| I(x) - \mathbf{w}^T G(x) \sum_{i=1}^{N} c_i u_i(x) \right|^2 dx \\ &= \sum_{i=1}^{N} \int_{\Omega_i} \left| I(x) - \mathbf{w}^T G(x) c_i \right|^2 dx \\ &= \sum_{i=1}^{N} \int_{\Omega} \left| I(x) - \mathbf{w}^T G(x) c_i \right|^2 u_i(x) dx \end{aligned} \tag{7}$$

By exchanging the order of summation and integration, we get

$$F(\mathbf{u}, \mathbf{c}, \mathbf{w}) = \int_{\Omega} \sum_{i=1}^{N} \left| I(x) - \mathbf{w}^T G(x) \mathbf{c}_i \right|^2 u_i(x) dx. \tag{8}$$

This expression of the energy F allows us to derive an effective energy minimization scheme described in Section 2.4. As a result of minimizing the energy $F(\mathbf{u}, \mathbf{c}, \mathbf{w})$, we obtain the optimal membership function $\hat{\mathbf{u}} = (\hat{u}_1, \cdots, \hat{u}_N)^T$ as the segmentation result, and the optimal vector $\hat{\mathbf{w}}$, from which the estimated bias field is computed by $b(x) = \hat{\mathbf{w}}^T G(x)$.

As will be shown in Section 2.4, the optimal membership functions $u_1, \cdots, u_N$ that minimize the energy defined in (8) are

binary functions, with values being either 0 or 1, which give a hard segmentation result. In many applications, it is preferable to have fuzzy (or soft) segmentation results, which are given by fuzzy membership functions that take values between 0 and 1 as in the fuzzy C-means (FCM) clustering method. To achieve fuzzy segmentation, we modify the energy function F in (8) by introducing a fuzzifier $q \geq 1$ to define the following energy:

$$F_q(\mathbf{u}, \mathbf{c}, \mathbf{w}) = \int_\Omega \sum_{i=1}^N \left| I(x) - \mathbf{w}^T G(x) c_i \right|^2 u_i^q(x) dx. \tag{9}$$

For the case $q > 1$, the optimal membership functions that minimize the energy F_q ($\mathbf{u}$, $\mathbf{c}$, $\mathbf{w}$) are fuzzy membership functions, which take value between 0 and 1.

Our method performs image segmentation and bias field estimation by minimizing the energy $F(\mathbf{u}, \mathbf{c}, \mathbf{w})$ in Eq. (8) or $F_q(\mathbf{u}, \mathbf{c}, \mathbf{w})$ in Eq. (9), subject to the constraints $\mathbf{u} \in \mathcal{U}$. A desirable property of this energy $F_q(\mathbf{u}, \mathbf{c}, \mathbf{w})$ is that it is convex in each variable, $\mathbf{u}$, $\mathbf{c}$, or $\mathbf{w}$. This property ensures that the energy $F_q(\mathbf{u}, \mathbf{c}, \mathbf{w})$ has a unique minimum point in each of its variables.

2.4. Energy minimization

The energy minimization can be achieved by alternately minimizing $F_q(\mathbf{u}, \mathbf{c}, \mathbf{w})$ with respect to each of its variables given the other two fixed. The minimization of $F_q(\mathbf{u}, \mathbf{c}, \mathbf{w})$ with respect to each of its variables is described below.

2.4.1. Optimization of $\mathbf{c}$
For fixed $\mathbf{w}$ and $\mathbf{u} = (u_1, \cdots, u_N)^T$, the energy $F(\mathbf{u}, \mathbf{c}, \mathbf{w})$ is minimized with respect to the variable $\mathbf{c}$. It is easy to show that $F(\mathbf{u}, \mathbf{c}, \mathbf{w})$ is minimized by $\mathbf{c} = \hat{\mathbf{c}} = (\hat{c}_1, \cdots, \hat{c}_N)^T$ with

$$\hat{c}_i = \frac{\int_\Omega I(x) b(x) u_i^q(x) dx}{\int_\Omega b^2(x) u_i^q(x) dx}, \quad i = 1, \cdots, N. \tag{10}$$

2.4.2. Optimization of $\mathbf{w}$ and bias field estimation
For fixed $\mathbf{c}$ and $\mathbf{u}$, we minimize the energy $F(\mathbf{u}, \mathbf{c}, \mathbf{w})$ with respect to the variable $\mathbf{w}$. This can be achieved by solving the equation $\frac{\partial F}{\partial \mathbf{w}} = 0$. It is easy to show that

$$\frac{\partial F}{\partial \mathbf{w}} = -2\mathbf{v} + 2A\mathbf{w}$$

where $\mathbf{v}$ is an M-dimensional column vector given by

$$\mathbf{v} = \int_\Omega G(x) I(x) \left(\sum_{i=1}^N c_i u_i^q(x) \right) dx, \tag{11}$$

where A is an M × M matrix

$$A = \int_\Omega G(x) G^T(x) \left(\sum_{i=1}^N c_i^2 u_i^q(x) \right) dx. \tag{12}$$

The equation $\frac{\partial F}{\partial \mathbf{w}} = 0$ can be expressed as a linear equation:

$$A\mathbf{w} = \mathbf{v} \tag{13}$$

Given the solution of this equation, $\hat{\mathbf{w}} = A^{-1}\mathbf{v}$, we compute the estimated bias field as $\hat{b}(x) = \hat{\mathbf{w}}^T G(x)$.

It can be shown that the matrix A is non-singular (see Section 2.5). Therefore, the linear equation $\frac{\partial F}{\partial \mathbf{w}} = -2\mathbf{v} + 2A\mathbf{w} = 0$ has a unique

solution $\hat{\mathbf{w}} = A^{-1}\mathbf{v}$. From (12), the vector $\hat{\mathbf{w}}$ can be explicitly expressed as

$$\hat{\mathbf{w}} = \left(\int_\Omega G(x) G^T(x) \left(\sum_{i=1}^N c_i^2 u_i^q(x) \right) dx \right)^{-1} \int_\Omega G(x) I(x) \left(\sum_{i=1}^N c_i u_i^q(x) \right) dx \tag{14}$$

With the optimal vector $\hat{\mathbf{w}}$ given by (14), the estimated bias field is computed by

$$\hat{b}(x) = \hat{\mathbf{w}}^T G(x) \tag{15}$$

In Section 2.5, we will prove the non-singularity of the matrix A and the numerical stability of the above computation for solving the linear system (13), which are two important issues in the implementation of our method.

2.4.3. Optimization of $\mathbf{u}$
We first consider the case of $q > 1$. For fixed $\mathbf{c}$ and $\mathbf{w}$, we minimize the energy $F(\mathbf{u}, \mathbf{c}, \mathbf{w})$ subject to the constraint that $\mathbf{u} \in \mathcal{U}$. It can be shown that $F(\mathbf{u}, \mathbf{c}, \mathbf{w})$ is minimized at $\mathbf{u} = \hat{\mathbf{u}} = (\hat{u}_1, \cdots, \hat{u}_N)^T$, given by

$$\hat{u}_i(x) = \frac{(\delta_i(x))^{\frac{1}{1-q}}}{\sum_{j=1}^N (\delta_j(x))^{\frac{1}{1-q}}}, \quad i = 1, \cdots, N, \tag{16}$$

where

$$\delta_i(x) = |I(x) - \mathbf{w}^T G(x) c_i|^2. \tag{17}$$

For $q = 1$, it can be shown that the minimizer $\hat{\mathbf{u}} = (\hat{u}_1, \cdots, \hat{u}_N)^T$ is given by

$$\hat{u}_i(x) = \begin{cases} 1, & i = i_{min}(x); \\ 0, & i \neq i_{min}(x). \end{cases} \tag{18}$$

where

$$i_{min}(x) = \arg\min_i \{\delta_i(I(x))\}.$$

2.5. Matrix analysis for numerical stability

The computation for the bias field estimation includes the computation of the vector $\mathbf{v}$ in (11), the matrix A in (12), and the inverse matrix A^{-1} in (14). The matrix A is an $M \times M$ matrix, with M being the number of basis functions. In this paper, we use $M = 20$ basis functions, and therefore the matrix A is an 20×20 matrix. It will be shown that the matrix A is non-singular, which ensures that the inverse matrix A^{-1} exists and the Eq. (13) has a unique solution. Furthermore, we will also show that the numerical computation of the inverse matrix A^{-1} is stable.

The non-singularity of matrix A given in Eq. (12) is verified as follows. We first define $h_m(x) \triangleq g_m(x) \sqrt{\sum_{i=1}^N c_i^2 u_i^q(x)}$. Thus, the (m, k) entry of the matrix A can be expressed as the inner product of h_m and h_k given by

$$\langle h_m, h_k \rangle = \int_\Omega h_m(x) h_k(x) dx.$$

Therefore, the matrix A is the Gramian matrix of $h_1, \cdots, h_M$. By linear algebra [28], the Gramian matrix of $h_1, \cdots, h_M$ is non-singular if and only if they are linearly independent. It is easy to see that the above defined functions $h_1, \cdots, h_M$ are linearly independent, which implies the non-singularity of A.

Numerical stability is an important issue in solving the Eq. (13). The numerical stability of solving the Eq. (13) is characterized by the condition number of the matrix A [29]. The condition number of a positive-definite matrix A is given by

$$\kappa(A) = \lambda_{max}(A)/\lambda_{min}(A),$$

where $\lambda_{min}(A)$ and $\lambda_{max}(A)$ are the minimal and maximal eigenvalues of matrix A, respectively. If the conditions number $\kappa(A)$ is very large, small variations in the matrix A or the vector $\mathbf{v}$, which likely occur due to the noise in the image and accumulating intermediate rounding errors, can cause very large variation of the solution $\hat{b\mathbf{w}}$ to the Eq. (13). Therefore, to ensure the robustness of the computation of the bias field, it is critical to ensure that the condition number $\kappa(A)$ is not large, which is verified as below.

The following matrix analysis is based on the orthogonality of the basis functions, namely,

$$\int_\Omega g_m(x)g_k(x)dx = \delta_{mk},\qquad(19)$$

where $\delta_{mk} = 0$ for $m \neq k$ and $\delta_{mk} = 1$ for $m = k$.

For the above defined matrix A in Eq. (12) with the basis functions $g_1, \cdots, g_M$ satisfying the orthogonality condition in Eq. (19), it can be shown that

$$0 < \min_i\left\{c_i^2\right\} \leq \lambda_{min}(A) \leq \lambda_{max}(A) \leq \max_i\left\{c_i^2\right\}$$

Therefore, the condition number of A is bounded by

$$\kappa(A) \leq \frac{\max_i\left\{c_i^2\right\}}{\min_i\left\{c_i^2\right\}}.\qquad(20)$$

For example, if $\max_i\{c_i\} = 250$ and $\min_i\{c_i\} = 50$, by the inequality (20), we have $\kappa(A) \leq \frac{250^2}{50^2} = 25$. In the applications of our method to real MRI data, we have found that the condition numbers of the matrix A are at this level, which is small enough to ensure the numerical stability of the inversion operation.

2.6. Implementation

From Section 2.4, we summarize the scheme of minimization of the energy $F_q(\mathbf{u}, \mathbf{c}, \mathbf{w})$ for $q \geq 1$ as the following iteration process:

• Step 1. Initialize $\mathbf{u}$ and $\mathbf{c}$;
• Step 2. Update b as $\hat{b}$ in (15).
• Step 3. Update $\mathbf{c}$ as $\hat{\mathbf{c}}$ in (10).
• Step 4. Update $\mathbf{u}$ as $\hat{\mathbf{u}}$ in (16) for the case $q > 1$ or (18) for the case $q = 1$;
• Step 5. Check convergence criterion. If convergence has been reached or the iteration number exceeds a prescribed maximum number, stop the iteration, otherwise, go to step 2.

In the above described iteration process, each of the three variables is updated with the other two variables computed in the previous iteration. Therefore, we only need to initialize two of the three variables, such as $\mathbf{u}$ and $\mathbf{c}$ in step 1 in the above iteration process. The convergence criterion used in step 5 is $|\mathbf{c}^{(n)} - \mathbf{c}^{(n-1)}| < \varepsilon$, where $\mathbf{c}^{(n)}$ is the vector $\mathbf{c}$ updated in step 3 at the n-th iteration, and ε is set to 0.001.

To demonstrate the robustness of our method to initialization, we applied it to a synthetic image in Fig. 1(a), with three different initializations of the membership functions $u_1, \cdots, u_N$ and the constants $c_1, \cdots, c_N$. The initial membership function $\mathbf{u} = (u_1, \cdots, u_N)$ and the vector $\mathbf{c} = (c_1, \cdots, c_N)$ can be visualized as an image defined by $J_{\mathbf{u},\mathbf{c}}(x) = \sum_{i=1}^{N} c_i u_i(x)$. The images $J_{\mathbf{u},\mathbf{c}}$ for the three different initializations of $\mathbf{u}$ and $\mathbf{c}$ are shown in Fig. 1(b), (c), and (d), which exhibit very different patterns. In particular, the first initialization shown in Fig. 1(b) is obtained by generating the membership functions $u_1(x), \cdots, u_N(x)$ and the constants $c_1, \cdots, c_N$ as random numbers. For these three different initializations of $\mathbf{u}$ and $\mathbf{c}$, the bias field converges to the same function up to a scalar multiple. By normalizing the bias fields (e.g. dividing the bias field b by its maximum value $\max_x\{b(x)\}$), the three estimated bias fields are the same, up to a negligible difference, which is shown in Fig. 1(e). Meanwhile, the membership function $\mathbf{u}$ converges to the same vector valued function, up to a negligible difference, yielding the same segmentation result as shown in Fig. 1(f). The bias field corrected image is shown in Fig. 1(g).

In Fig. 1(h), we plot the energy $F(\mathbf{u}, \mathbf{c}, \mathbf{w})$ of the variables $\mathbf{u}$, $\mathbf{c}$, and $\mathbf{w}$ computed at each iteration for 20 iterations. It is clearly seen that, the energy $F(\mathbf{u}, \mathbf{c}, \mathbf{w})$ decreases rapidly to the same value from three different initial values corresponding to the three different initializations. This figure also demonstrates fast convergence of the iteration in MICO, as we can clearly see that the energy is rapidly decreased and converge to the minimum value in less than 10 iterations. Therefore, we usually only perform 10 iterations in our applications of MICO.

3. Some extensions

3.1. Introduction of spatial regularization in MICO

The basic MICO formulation presented above can be readily built upon to add a regularization term on the membership functions. Based on the MICO formulation, regularization of the membership functions can be achieved by adding the total variations (TV) of the membership functions in the following energy:

$$\mathcal{F}(\mathbf{u}, \mathbf{c}, \mathbf{w}) = \lambda F(\mathbf{u}, \mathbf{c}, \mathbf{w}) + \sum_{i=1}^{N} TV(u_i),\qquad(21)$$

where F is the energy defined in (8), $\lambda > 0$ is the weight of F, and TV is the total variations of u defined by

$$TV(u) = \int_\Omega |\nabla u(x)|dx.\qquad(22)$$

This energy should be minimized subject to the constraint that $0 \leq u_i(x) \leq 1$ and $\sum_{i=1}^{N} u_i(x) = 1$ for every point x. The variational formulation in (21) is referred to by *TVMICO* formulation. The definition of this energy (21) is simple, but in the energy minimization, it is not trivial to deal with the above point wise constraint.

In recent years, many researchers have proposed various numerical schemes [30] to solve the variational problems in the context of image segmentation with a TV regularization term $TV(u)$ for a membership function u subject to the constraint $0 \leq u(x) \leq 1$. These methods are only able to segment the images into two complementary regions, which are represented by the membership functions u and 1-u. In general, for segmentation of $N > 2$ regions, three or more membership functions $u_1, \cdots, u_N$ are used to represent $N > 2$ regions. In [31], Li et al. used the operator splitting method proposed by Lions and Mercier in [32] to develop a numerical scheme to solve the energy minimization problem with TV regularization on the membership functions as in (21). The minimization of the energy $\mathcal{F}$ with respect to the membership functions $u_1, \cdots, u_N$ in (21) can be performed by using the numerical scheme described in [31]. The energy minimizations with respect to the variables $\mathbf{c}$ and $\mathbf{w}$, which are independent of the TV

regularization term of the membership functions, remain the same as described in Section 2.4.

3.2. Spatiotemporal regularization for 4D segmentation

The TVMICO formulation in (21) can be further extended to 4D MICO with spatiotemporal regularization of the tissue membership functions for segmentation of 4D data, which is a series of 3D scans of the same subject at different time points. While the basic MICO formulation presented in Section 2 allows for various 4D extensions with different spatiotemporal regularization mechanisms, we only provide a simple and natural 4D extension of the basic MICO formulation in the following as an example.

Before we present the 4D MICO formulation, we first describe a model of serial MR images captured from the same subject at different time points. We assumed that all the images in a longitudinal series are registered to the first image in the series by using rigid registration with six degree of freedom. Therefore, all the registered images in the series are in a common space, denoted by Ω, which can be represented by a 4D image $I(x, t)$ with spatial variable $x \in \Omega$ and temporal variable t in a time period $[0, L]$. The series of images $I(\cdot, t)$ can be modeled as

$$I(x, t) = b(x, t)J(x, t) + n(x, t) \tag{23}$$

where $J(\cdot, t)$ is the true image, and $b(\cdot, t)$ is the bias field, and $n(\cdot, t)$ is additive noise.

We assume there are N types of tissues in the image domain Ω. The true image $J(x, t)$ can be approximated by $J(x, t) = \sum_{i=1}^{N} c_i(t) u_i(x, t)$, where N is the number of tissues in Ω, and $u_i(\cdot, t)$ is the membership function of the i-th tissue, and the constant $c_i(t)$ is the value of the true image $J(x, t)$ in the i-th tissue. For convenience, we represent the constants $c_1(t), \cdots, c_N(t)$ with a column vector $c(t) = (c_1(t), \cdots, c_N(t))^T$. The membership functions $u_1(x, t), \cdots, u_N(x, t)$ are also represented by a vector-valued function $\mathbf{u}(x, t) = (u_1(x, t), \cdots, u_N(x, t))^T$.

The bias field $b(\cdot, t)$ at each time point t is estimated by a linear combination of a set of smooth basis functions $g_1(x), \cdots, g_M(x)$. Using the vector representation in Section 2, the bias field $b(\cdot, t)$ at the time point t can be expressed as

$$b(x, t) = \mathbf{w}(t)^T G(x), \tag{24}$$

a) Original image.　b) Initialization 1.　c) Initialization 2.　d) Initialization 3.

e) Estimated bias field.　f) Segmentation re-sult.　g) Bias field cor-rected image.
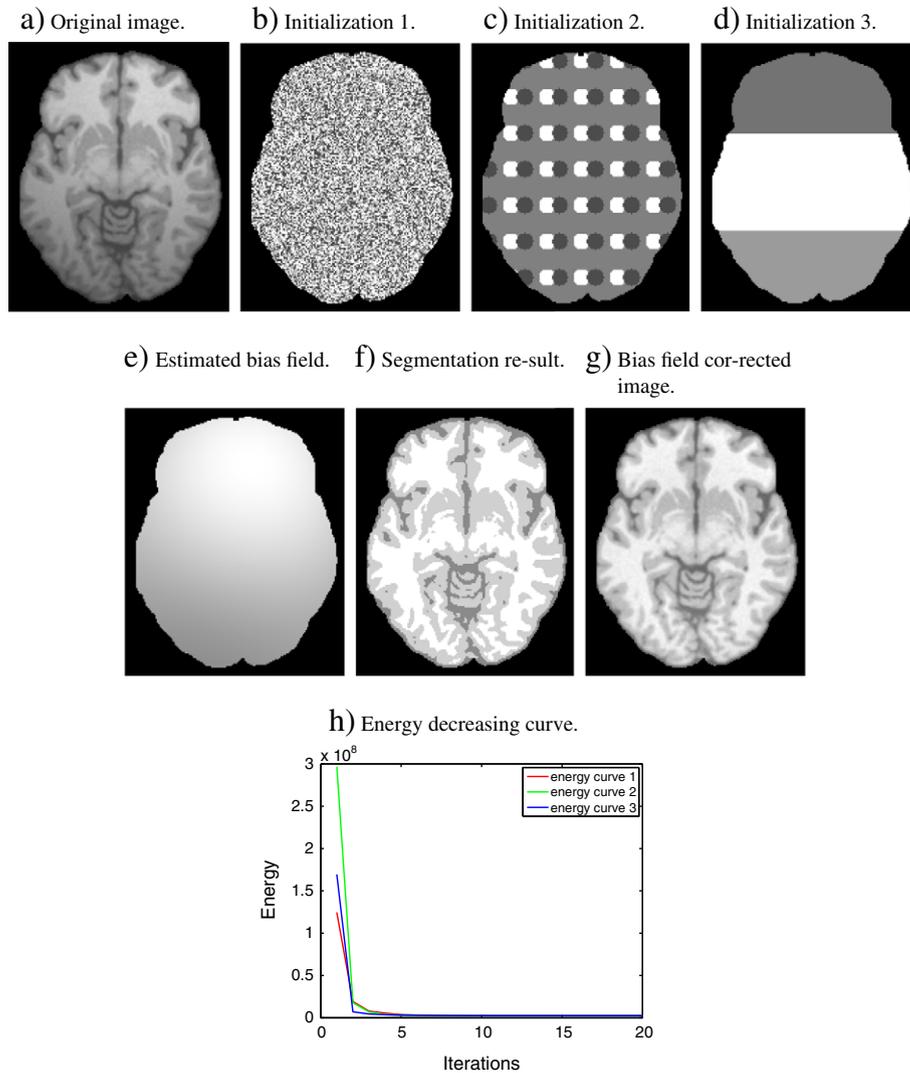
h) Energy decreasing curve.

Fig. 1. Demonstration of robustness of our method to initialization. (a) Original image; (b)–(d) Visualization of three different initializations of the membership functions; (e) Estimated bias field; (f) Segmentation result; (g) Bias corrected image; (h) Curves showing the energy F in the iteration process from three different initializations shown in (b), (c), and (d).
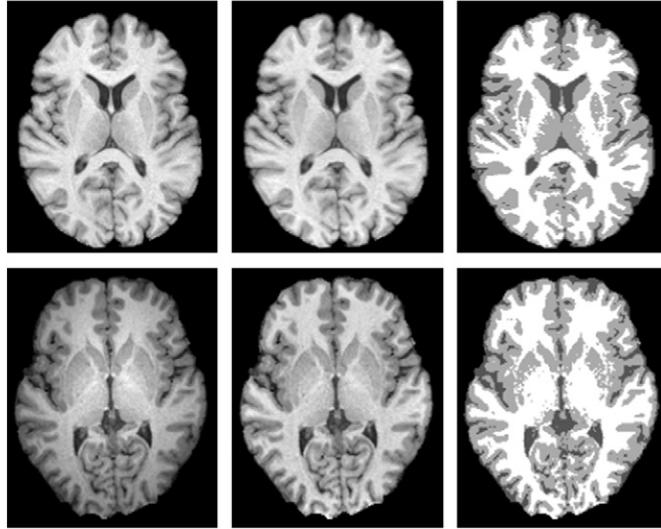
Fig. 2. Bias correction and tissue segmentation results of our method on the data from 1.5 T (upper row) and 3 T (lower row) MR scanners. The left, middle, and right columns show the original images, bias field corrected image, and segmentation results, respectively.

with $\mathbf{w}(t) = (w_1(t), \cdots, w_M(t))^T$, where $w_1(t), \cdots, w_M(t)$ are the time dependent coefficients of the basis function $g_j(x)$, $j = 1, \cdots, M$.

The spatiotemporal regularization of the membership functions $u_i(x,t)$ can be naturally taken into account in the following variational formulation with a data term (image based term) and a spatiotemporal regularization term as follows:

$$\mathcal{G}(\mathbf{u}, \mathbf{c}, \mathbf{w}) = \lambda \int_{[0,L]} F(\mathbf{u}(\cdot, t), \mathbf{c}(t), \mathbf{w}(t))dt + \sum_{i=1}^{N} TV(u_i) \qquad (25)$$

where $\lambda > 0$ is a constant, $F(\mathbf{u}(\cdot,t), \mathbf{c}(t), \mathbf{w}(t))$ is the data term defined in (8) for the image $I(\cdot,t)$ at the time point t, namely,

$$F(\mathbf{u}(\cdot, t), \mathbf{c}(t), \mathbf{w}(t)) = \int_{\Omega} \sum_{i=1}^{N} \left| I(x,t) - \mathbf{w}(t)^T G(x)c_i(t) \right|^2 u_i^q(x,t)dx,$$

and $TV(u_i)$ is the spatiotemporal regularization term on the membership function $\mathbf{u}$, which can be expressed as:

$$TV(u_i) = \int |\nabla u_i(x,t)| dxdt, \qquad (26)$$

where the gradient operator ∇ is with respect to the spatial and temporal variables x and t. We call the above variational formulation a 4D MICO formulation.

The minimization of the energy $\mathcal{G}$ is subject to the constraints on the membership function. Therefore, we solve the following constrained energy minimization problem:

$$\begin{aligned} \text{Minimize} \quad & \mathcal{G}(\mathbf{u}, \mathbf{c}, \mathbf{w}) \\ \text{subject to} \quad & 0 \le u_i(x) \le 1, i = 1, \cdots, N, \text{ and } \sum_{i=1}^{N} u_i(x) = 1 \end{aligned} \qquad (27)$$

The minimization of the energy $\mathcal{G}$ with respect to $\mathbf{c}(t)$ and $\mathbf{w}(t)$ is independent of the spatiotemporal regularization term in (25). The optimal vectors $\mathbf{c}(t)$ and $\mathbf{w}(t)$ can be computed for each time point t independently from the image $I(\cdot,t)$ as in the energy minimization for the basic MICO formulation described in Section 2.4. The minimization of $\mathcal{G}$ with respect to the 4D membership function $\mathbf{u}$ subject to the constraint in (27) can be achieved by using the numerical scheme in [31] for variational formulations with TV regularization. The detailed description of the numerical scheme for

solving the constrained energy minimization problem in (27) and its modified forms will be provided in our future publication that focuses on 4D segmentation based on the basic MICO formulation.

3.3. Modified MICO formulation with weighting coefficients for different tissues

The basic MICO formulation in Section 2 can be modified by introducing weighting coefficients $\lambda_1, \cdots, \lambda_N$ for the N tissues in the definition of the energy function $F(\mathbf{u}, \mathbf{c}, \mathbf{w})$ in Eq. (8). We defined the modified energy as

$$F(\mathbf{u}, \mathbf{c}, \mathbf{w}) = \int_{\Omega} \sum_{i=1}^{N} \lambda_i \left| I(x) - \mathbf{w}^T G(x)c_i \right|^2 u_i^q(x)dx, \qquad (28)$$

where λ_i is the coefficient for the i-th tissue.

The introduction of the parameters $\lambda_1, \cdots, \lambda_N$ provides an option for the users to improve the results of the basic MICO formulation in 2. For example, if the i-th tissue is over segmented by using the basic MICO formulation in Section 2, one can use the above modified formulation in (28) with a larger $\lambda_i > 1$.

4. Results and discussions

Our method has been extensively tested on synthetic and real MRI data, including 1.5 T and 3 T MRI data. In this section, we first show experimental results of our method for some synthetic and real MR images, including some images with severe intensity inhomogeneities. We also present the results of quantitative evaluation and comparisons with some popular methods.

In our applications of MICO of 1.5 T and 3 T MR images, we use 20 polynomials of the first three orders as the basis functions $g_1, \cdots, g_M$ with $M = 20$. Our method with these 20 basis functions works well for images acquired from 1.5 T and 3 T MRI scanners. For higher field (e.g. 7 T) MRI scanners, the intensity inhomogeneities have more complicated profiles than 1.5 T and 3 T MR images. In this situation, more basis functions are needed so that a larger range of bias fields can be well approximated by their linear combinations. Theoretically, any function can be well approximated by a linear combination of a set of basis functions up to arbitrary accuracy [27], given a sufficiently large number of basis functions. The numerical
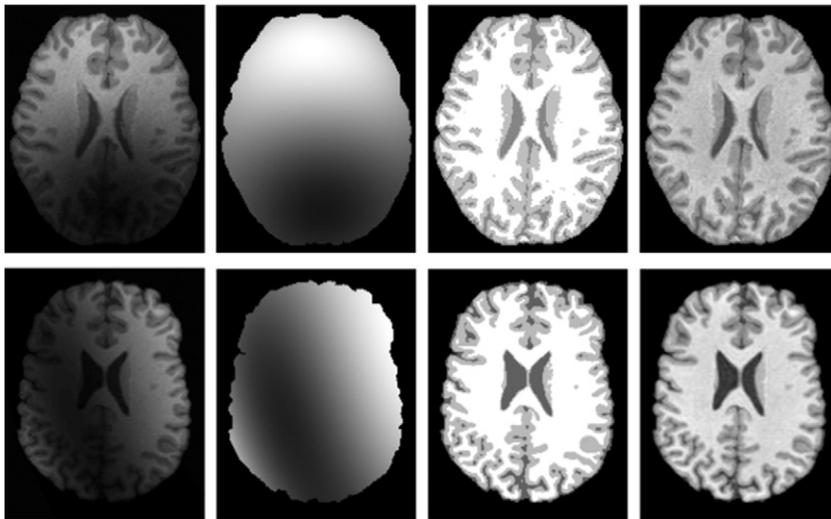
Fig. 3. Results for images with severe intensity inhomogeneity shown in the left column. The estimated bias fields, segmentation results, and bias field corrected images are shown in columns 2, 3, 4, respectively.

stab + ility of the computation of the inverse matrix A^{-1} in (14), with A being an $M \times M$ matrix, is an important numerical issue, especially for a large M. Fortunately, by the matrix analysis in Section 2.5, we have shown that the condition number of the matrix A is bounded by a constant as in (20), which is independent of the number of basis functions. This ensures the numerical stability of the computation of the bias field, regardless of how many basis functions are used.

We have applied MICO to 1.5 T and 3 T MRI data with desirable results. For examples, we show the bias field correction and segmentation results of our method for a 1.5 T and a 3 T MR images in Fig. 2. The original images, the bias field corrected images, and the segmentation results are shown in the left, middle, and the right columns, respectively. To demonstrate the ability of our method to deal with severe intensity inhomogeneities, we applied MICO to the two images in the left column in Fig. 3. The estimated bias field, the segmentation results, and the bias field corrected images obtained by our method are shown in the second, third, and fourth columns, respectively. Despite the severe intensity inhomogeneities in the

images, our method is able to produce desirable results of bias field correction and tissue segmentation as shown in Fig. 3.

In the following experiment, we quantitatively evaluate and compare the segmentation accuracy of our method and the well-known softwares FSL, SPM, and FANTASM. These three softwares can be downloaded from http://www.fmrib.ox.ac.uk/fsl/ (for FSL), http://www.fil.ion.ucl.ac.uk/spm/software/ (for SPM), and http://mipav.cit.nih.gov/ (for FANTASM), respectively. The data used in our quantitative evaluation are downloaded from BrainWeb in [33]. BrainWeb also provides ground truth, which can be used to quantitatively evaluate segmentation accuracy.

Note that the intensity inhomogeneities generated by BrainWeb are linear, which are relatively easy to be handled. To examine the performance of segmentation algorithms in a more difficult situation, we generated simulated MR images with non-linear intensity inhomogeneities as follows. The degree of intensity inhomogeneity is indicated by the range of values of the bias field in the interval $[1 - \alpha, 1 + \alpha]$ with $\alpha > 0$. We generated five sets of images with $\alpha = 0.1, 0.2, 0.3, 0.4,$ and 0.5. For each α, we generated
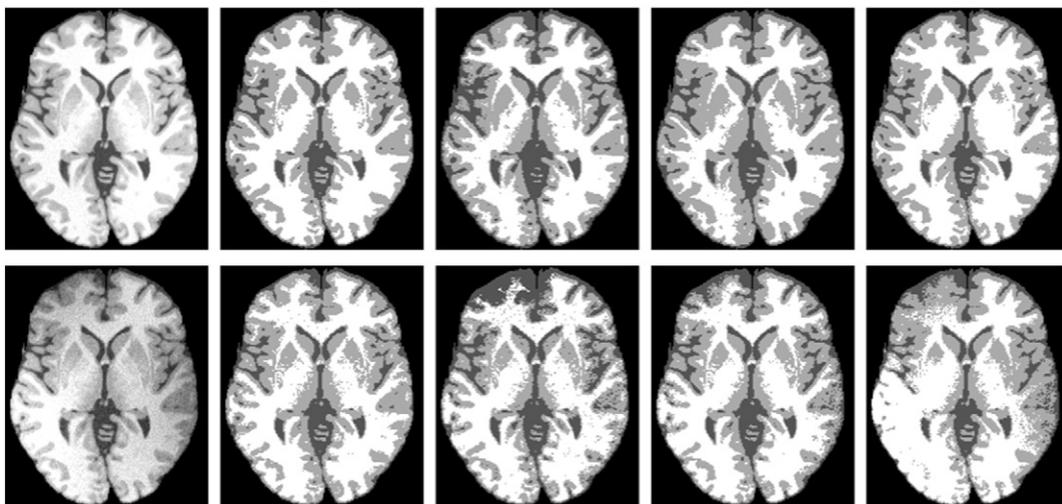

Fig. 4. Comparison of our method with SPM, FSL, FANTASM on synthetic images with different degrees of intensity inhomogeneities. The input images are shown in the left column, including an image with low degree of intensity inhomogeneity (in the upper row) and an image with high degree of intensity inhomogeneity (in the lower row). The corresponding segmentation results of our method, SPM, FSL, and FANTASM are shown in the second, third, fourth, and fifth columns, respectively.
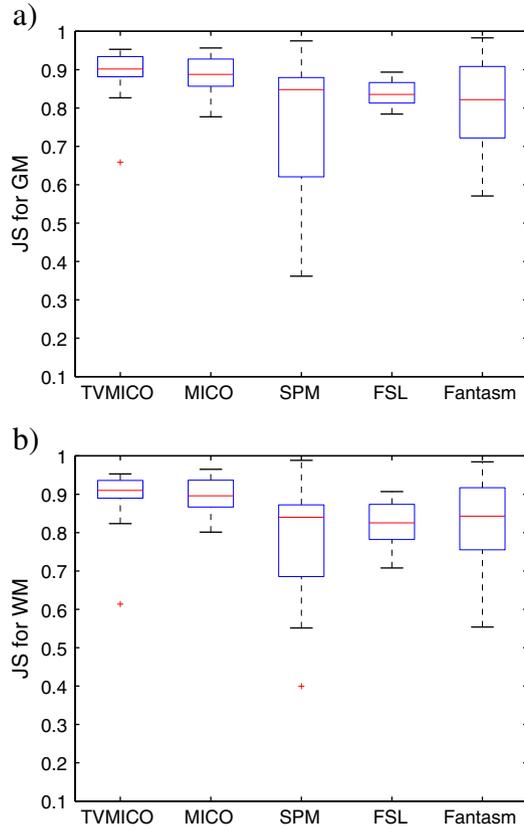
a)

b)

Fig. 5. Quantitative evaluation for the segmentation results of TVMICO (with $\lambda = 0.01$), MICO, SPM, FSL, and FANTASM for 30 images using Jarcard similarity with ground truth.

six different bias fields with values in $[1 - \alpha, 1 + \alpha]$ and multiplied them with the original image downloaded from BrainWeb to obtain six images with different intensity inhomogeneities. Then we added noise of six different levels to these images. Thus, there are 30 images in the five sets of images with different degrees of intensity inhomogeneities and different levels of noise. In Fig. 4, we first show the segmentation results of the four tested methods for two of the 30 images, one with the lowest degree of intensity inhomogeneity

(generated with $\alpha = 0.1$) and the other one the highest degree of intensity inhomogeneity (generated with $\alpha = 0.5$). For the image with low degree of intensity inhomogeneity, the segmentation results of the four methods look similar by visual comparison, as shown in the upper row in Fig. 4. The advantage of our method is particularly noticeable for the image with high degree of intensity inhomogeneity, as shown in the lower row in Fig. 4.

More objective and precise comparison of the segmentation accuracy of the four segmentation methods can be performed by evaluating the segmentation results using the Jaccard similarity (JS) index [34], which is defined as

$$J(S_1, S_2) = \frac{|S_1 \cap S_2|}{|S_1 \cup S_2|} \tag{29}$$

where $|\cdot|$ represents the area of a region, S_1 is the region segmented by an algorithm, and S_2 is the corresponding region obtained from a reference segmentation result or the ground truth. For synthetic data from the BrainWeb, we have the ground truth of the segmentation of the WM, GM, and CSF, which can be directly used as S_2 in (29) to compute the JS index. The larger the JS value, the closer of the algorithm segmentation to the reference segmentation.

Fig. 5 shows the comparison of JS values of the four methods on the 30 synthetic images with different degrees of intensity inhomogeneities and different levels of noise, as described above. Fig. 5 shows the box plot of the JS values for the GM and WM obtained from our method (MICO and TVMICO), SPM, FSL, and FANTASM. From the box plot of the JS values in Fig. 5, it is clearly seen that both MICO and TVMICO have better performance than SPM, FSL, and FANTASM in terms of segmentation accuracy and robustness.

We note that the box shown in the box plot for the basic MICO is relatively shorter and there are no outliers in the JS values for all the 30 test images. This exhibits desirable robustness of the basic MICO. The TVMICO has slightly better accuracy than the basic MICO, but there are outliers in the JS values for TVMICO. The performance of TVMICO depends on the choice of the parameter λ in (21), which need to be tuned for some cases. In this experiment, we fixed $\lambda = 0.01$ for all the 30 test images, and we found that the results are overall desirable except one case, which leads to the outliers in the box plot in Fig. 5. By comparison, the basic MICO is more robust, and the performance is more stable than TVMICO, while the latter is slightly more accurate than the former except for most of the cases.
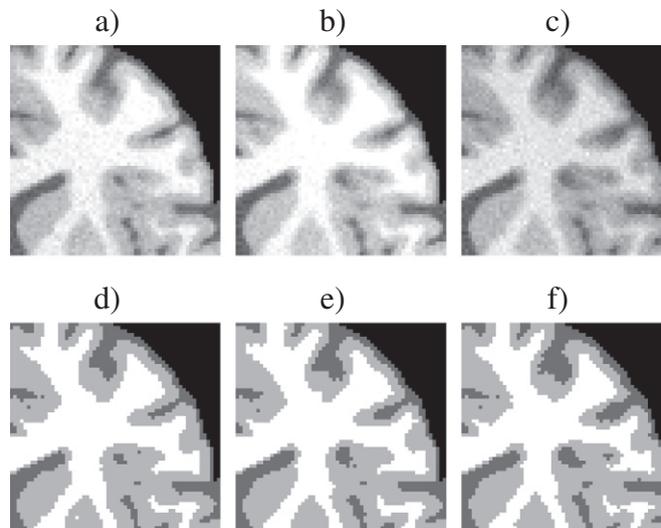

Fig. 6. An example of the application of 4D MICO to a synthetic longitudinal data with simulated atrophy.

In fact, for images with reasonable noise level, the difference of the segmentation accuracy of MICO and TVMICO is not significant. We suggest that the basic MICO be used when robustness is a priority or the noise level in the images is not high. Especially for fully automatic segmentation of large data sets, the robustness and stability of performance is a major concern, and the basic MICO is preferable to TVMICO for its robustness and stable performance.

The 4D MICO algorithm has been tested on synthetic data with promising results. We generated a synthetic longitudinal data with simulated atrophy by using the atrophy simulator developed in [35]. The atrophy simulator simulates the atrophy by shrinking the GM and WM and expanding CSF in the input MR image at a specified rate and location, and of a specified size. Based on the images obtained from the atrophy simulator, we added different intensity inhomogeneities and noise to them to test the performance of our method in the presence of intensity inhomogeneities and noise. We used this synthetic data to test the ability of the 4D MICO to capture subtle changes caused by the atrophy.

The upper row of Fig. 6 shows a portion of the brain in images of three consecutive time points. This portion of the images contains the atrophy simulated by the atrophy simulator. These images exhibit subtle expanding of CSF and shrinking of WM and GM near the cortex, and the same brain tissue structure in the rest of this portion. The results of the 4D MICO, shown in the lower row of Fig. 6, indeed agree with structural changes caused by the simulated atrophy in these three images, while the segmented tissues in the non-atrophy region remain almost the same in these three images. This experiment shows the temporal consistency of our method and the ability to capture subtle changes caused by atrophy or other biological changes.

In this experiment, we used $\lambda = 0.008$ in the 4D MICO formulation in (25). We have noticed that the performance of the 4D MICO formulation in (25) depends on the choice of the parameter λ and some additional parameters in the numerical scheme for energy minimization with respect to the membership functions. More details about the implementation and validations of the 4D MICO formulation in (25) and its modified forms will be presented in our future publication as an extension of this paper.

The estimated bias field $\hat{b}$ of MICO can be used to compute the bias field corrected image $I/\hat{b}$. We have evaluated the performance of bias field correction of MICO and compared it with two well-known bias field correction methods, namely, N3 method proposed in [17] and entropy minimization method in [21]. The performance of bias field correction can be evaluated by quantifying the intensity inhomogeneities of the bias field corrected images using the coefficient of variations (CV) and coefficient of joint variation (CJV). For each tissue T (WM or GM), the CV is defined by

$$CV(T) = \frac{\sigma(T)}{\mu(T)},$$

where $\sigma(T)$ and $\mu(T)$ are the standard deviation and the mean of the intensities in the tissue T. The CJV is defined as

$$CJV = \frac{\sigma(WM) + \sigma(GM)}{|\mu(WM) - \mu(GM)|}.$$

The performance of bias field correction is evaluated by the CV and CJV of the bias field corrected images, with smaller CV and CJV values indicating better bias field correction results.

We applied our method and the N3 and entropy minimization methods implemented in the MIPAV software to 15 images acquired from 3 Tesla MRI scanners. The MIPAV software is publicly available in http://mipav.cit.nih.gov/. The CV and CJV values of the three tested methods for the 15 images are plotted in Fig. 7, which

shows better performance of our method than N3 and entropy minimization methods.

Note that, in the standard definition of CV and CJV in the literature on bias field correction [5], the GM and WM are the ground truth. Since we do not have the ground truth of GM and WM for the real MR images, we used an approximate of the ground truth of GM/WM by the intersection of the segmented GM/WM obtained by applying K-means algorithm to the bias corrected images by the three compared bias field correction methods: our method and the well-known N3 method [17] and the entropy minimization method [21].

As mentioned earlier, we only used 20 polynomials as the basis functions in the estimation of the bias field. It can be expected
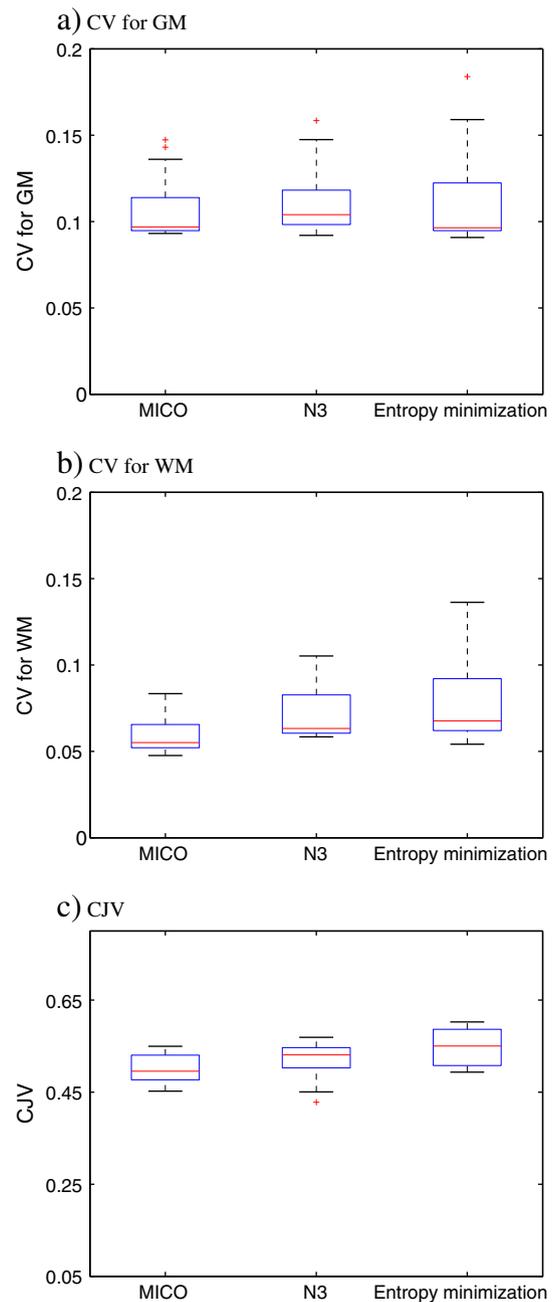

Fig. 7. Comparison of the performance of bias field correction of our method, N3 algorithm, and entropy minimization method in terms of CV and CJV for 15 images from 3 T MR scanners.

that the capability of the bias field correction of MICO can be enhanced by using more and different types of basis functions, such as the B-spline functions, which would increase the range of bias fields represented by the linear combinations of the basis functions. This would enable the application of MICO to ultra high field MRI (e.g. 7 Tesla) and other medical images with more severe intensity inhomogeneities.

5. Conclusion

We have proposed a principled method, called multiplicative intrinsic component optimization (MICO), for bias field estimation and segmentation of MR images in a new energy minimization formulation. By calculus of matrix and vector, we have derived an efficient energy minimization scheme for the computation of the bias field, and used matrix analysis to verify the numerical stability of the computation for the optimization of the bias field. The robustness, accuracy, and efficiency of our method are demonstrated by the evaluation and comparison with other methods on synthetic and real MR data. Our method has been successfully applied to 1.5 T and 3 T MR images with desirable results. Experimental results have shown desirable advantages of our method in terms of segmentation accuracy and robustness, compared with popular softwares. In addition, we have shown that the basic MICO formulation can be naturally extended to 3D/4D segmentation with spatial/spatiotemporal regularization with promising result.

Acknowledgment

References

[1] Wells W, Grimson E, Kikinis R, Jolesz F. Adaptive segmentation of MRI data. IEEE Trans Med Imaging 1996;15(4):429–42.
[2] Guillemaud R, Brady J. Estimating the bias field of MR images. IEEE Trans Med Imaging 1997;16(3):238–51.
[3] Styner M, Brechbuhler C, Szekely G, Gerig G. Parametric estimate of intensity inhomogeneities applied to MRI. IEEE Trans Med Imaging 2000;19(3):153–65.
[4] Leemput V, Maes K, Vandermeulen D, Suetens P. Automated model-based bias field correction of MR images of the brain. IEEE Trans Med Imaging 1999;18(10):885–96.
[5] Vovk U, Pernus F, Likar B. A review of methods for correction of intensity inhomogeneity in MRI. IEEE Trans Med Imaging 2007;26(3):405–21.
[6] Pham D, Prince J. Adaptive fuzzy segmentation of magnetic resonance images. IEEE Trans Med Imaging 1999;18(9):737–52.
[7] Pham D. Spatial models for fuzzy clustering. Comput Vis Image Underst 2001;84(2):285–97.
[8] Condon BR, Patterson J, Wyper D. Image nonuniformity in magnetic resonance imaging: its magnitude and methods for its correction. Br J Radiol 1987;60(1):83–7.
[9] Simmons A, Tofts PS, Barker GJ, Arrdige SR. Sources of intensity nonuniformity in spin echo images at 1.5 t. Magn Reson Med 1991;32(1):121–8.
[10] Wicks DAG, Barker GJ, Tofts PS. Correction of intensity nonuniformity in MR images of any orientation. Magn Reson Imaging 1993;11(2):183–96.
[11] Tincher M, Meyer CR, Gupta R, Williams DM. Polynomial modeling and reduction of rf body coil spatial inhomogeneity in MRI. IEEE Trans Med Imaging 1993;12(2):361–5.
[12] Axel L, Costantini J, Listerud J. Intensity correction in surface-coil MR imaging. Am J Radiol 1987;148(2):418–20.
[13] McVeigh ER, Bronskil MJ, Henkelman RM. Phase and sensitivity of receiver coils in magnetic resonance imaging. Med Phys 1986;13(6):806–14.
[14] Narayana PA, Brey WW, Kulkarni MV, Sivenpiper CL. Compensation for surface coil sensitivity variation in magnetic resonance imaging. Magn Reson Imaging 1988;6(3):271–4.
[15] Johnston B, Atkins MS, Mackiewich B, Anderson M. Segmentation of multiple sclerosis lesions in intensity corrected multispectral MRI. IEEE Trans Med Imaging 1996;15(2):154–69.
[16] Dawant B, Zijdenbos A, Margolin R. Correction of intensity variations in MR images for computer-aided tissues classification. IEEE Trans Med Imaging 1993;12(4):770–81.
[17] Sled J, Zijdenbos A, Evans A. A nonparametric method for automatic correction of intensity nonuniformity in MRI data. IEEE Trans Med Imaging 1998;17(1):87–97.
[18] Ahmed M, Yamany S, Mohamed N, Farag A, Moriarty T. A modified fuzzy c-means algorithm for bias field estimation and segmentation of MRI data. IEEE Trans Med Imaging 2002;21(3):193–9.
[19] Salvado O, Hillenbrand C, Wilson D. Correction of intensity inhomogeneity in MR images of vascular disease. EMBS'05. Shanghai: IEEE; 2005. p. 4302–5.
[20] Li C, Huang R, Ding Z, Gatenby C, Metaxas D, Gore J. A variational level set approach to segmentation and bias correction of medical images with intensity inhomogeneity. Proc.Medical Image Computing and Computer Aided Intervention (MICCAI), Vol. LNCS 5242, Part II; 2008. p. 1083–91.
[21] Likar B, Viergever M, Pernus F. Retrospective correction of MR intensity inhomogeneity by information minimization. IEEE Trans Med Imaging 2001;20(12):1398–410.
[22] Tustison N, Avants B, Cook P, Zheng Y, Egan A, Yushkevich P, et al. N4itk: improved n3 bias correction. IEEE Trans Med Imaging 2010;29(6):1310–20.
[23] Barrow H, Tenenbaum J. Recovering intrinsic scene characteristics from images. In: Hanson A, Riseman E, editors. Computer Vision Systems. Academic Press; 1978. p. 3–26.
[24] Tappen M, Freeman W, Adelson E. Recovering intrinsic images from a single image. IEEE Trans Pattern Anal Mach Intell 2005;27(9):1459–72.
[25] Weiss Y. Deriving intrinsic images from image sequences. Proc. 8th International Conference on Computer Vision (ICCV), vol. II; 2001. p. 68–75.
[26] Kimmel R, Elad M, Shaked D, Keshet R, Sobel I. A variational framework for retinex. Int J Comput Vis 2003;52(1):7–23.
[27] Powell MJD. Approximation theory and methods. Cambridge: Cambridge University Press; 1981.
[28] Horn R, Johnson C. Matrix analysis. Cambridge: Cambridge University Press; 1985.
[29] Golub G, Loan CV. Matrix computations. 3rd ed. The Johns Hopkins University Press; 1996.
[30] T. Goldstein, S. Osher, The split bregman method for L1 regularized problems, UCLA CAM Report 2004, 08-29.
[31] Li F, Ng M, Li C. Variational fuzzy Mumford-Shah model for image segmentation. SIAM J Appl Math 2010;70(7):2750–70.
[32] Lions P, Mercier B. Splitting algorithms for the sum of two nonlinear operators. SIAM J Numer Anal 1979;16(6):964–79.
[33] http://www.bic.mni.mcgill.ca/brainweb/.
[34] Shattuck DW, Sandor-Leahy SR, Schaper KA, Rottenberg DA, Leahy RM. Magnetic resonance image tissue classification using a partial volume model. Neuroimage 2001;13:856–76.
[35] Karacali B, Davatzikos C. Simulation of tissue atrophy using a topology preserving transformation model. IEEE Trans Med Imaging 2006;25(5):649–52.